Optical CubeSat Discrimination

Doyle Hall
Boeing LTS / AMOS, Kihei, HI and Colorado Springs, CO

1 SUMMARY

Groups of CubeSats launched from the same upper stage vehicle often have identical size and other similarities in gross structure. However, these satellites often deploy a mission-specific configuration of wire antennas and/or cylindrical boom structures which can serve as unique identifiers. Such structures readily glint sunlight which create tell-tale photometric patterns that can reveal their size and orientation with respect to the main cubical body and provide a means of CubeSat characterization and discrimination.

2 INTRODUCTION

The numbers and capabilities of small cubical satellites have increased significantly during the past few years. Built by a variety of US and non-US academic, commercial and military organizations, such "CubeSats" typically occupy low-Earth orbits (LEO) and have mission lifetimes spanning from weeks to years. Most are nearly perfectly cubical, although some have elongated "shoebox" shapes. They are often launched in groups inserted into LEO almost simultaneously from the same launch vehicle. This creates a significant need for remote methods of discriminating one from another. Each of the eight edges of a typical CubeSat spans 10 to 30 cm, subtending 0.1–0.3 μrad (0.02–0.06 arcsec) when viewed by a sensor at a range of 1000km — too small to be resolved by even the most advanced ground-based optical and radar imaging instrumentation. This work discusses non-imaging methods of optical CubeSat discrimination, focusing specifically on using temporal photometry of reflected sunlight. Different CubeSats launched within a group often have many similarities in structure. For instance, solar arrays typically cover all or most of the six main faces, so gross photometric differences from main-face reflections generally cannot be used to distinguish one CubeSat from another. However, our analysis indicates that CubeSats often deploy wire antennas and/or cylindrical boom structures after orbital insertion. These deployed structures can serve as unique identifiers for these otherwise nearly identical objects, because each satellite's specific mission drives their exact configuration. Furthermore, because such cylindrical structures readily glint sunlight, they create tell-tale photometric patterns that can reveal their specific orientation with respect to the main cubical body, thereby providing a means of using temporal photometry of reflected sunlight for CubeSat characterization and discrimination.

3 METHODS OF SATELLITE DISCRIMINATION

Many traditional methods of optical satellite discrimination fail to distinguish many CubeSats. Ground-based imagery fails because most are not resolvable. Perhaps the simplest means of non-imaging discrimination, using the measured brightness of a satellite to estimate its size, fails because CubeSats launched in groups often have identical sizes or very similar bulk dimensions. Another relatively simple discrimination method, based on using brightness variations to evaluate the satellite's attitude (i.e., stabilized vs. rotating) also fails because many CubeSats are not actively stabilized and inserted into orbit with similar initial rotational parameters that are not known *a priori*. Spectroscopic methods also can fail because of the identical or similar nature of surface materials used to cover the six main cube faces.

Often different academic, commercial and military organizations sponsor one or sometimes two CubeSats launched within the same group. Each of these typically deploys a mission-specific configuration of antennas and booms. These can serve as unique identifiers because such cylindrical structures readily glint sunlight and create tell-tale photometric patterns. Figure 1 shows several images of typical CubeSats taken from the world-wide web. Even this relatively small sample of CubeSats shows a wide variety of configurations for the deployed antenna and boom structures. Most are linear cylinders, but some have curvature along their long dimension. Among the linear structures, some have their long axes oriented normal to one of the six main faces of the cubical body, while others are aligned radially outward. Some are attached to an edge or vertex of the cube while others to a point well within one of the six cube faces.

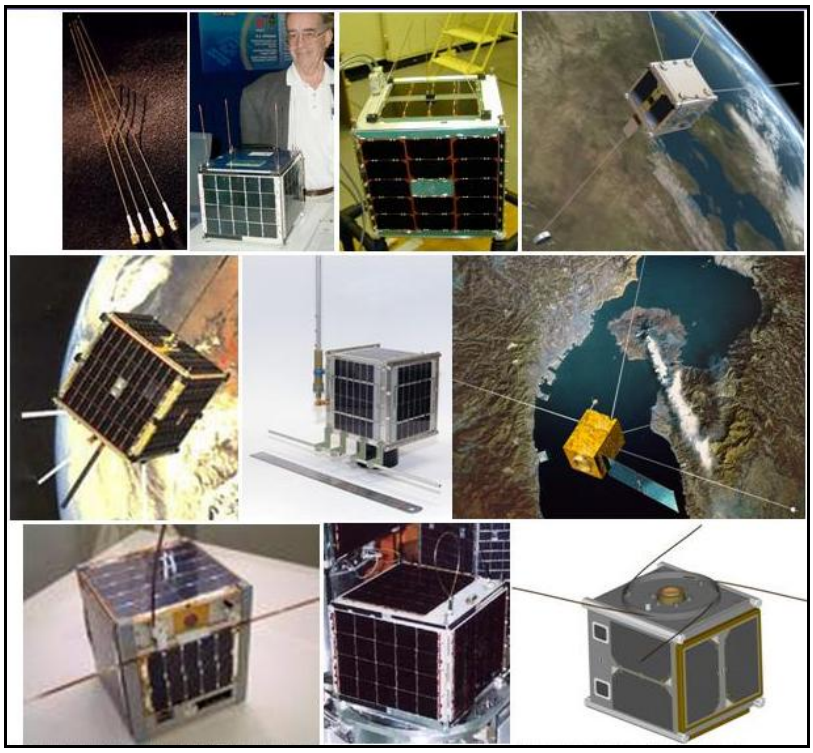

Figure 1. CubeSat antennas and booms. The upper left panel shows an isolated picture of four cylindrical metallic antennas typical for CubeSats. The remaining nine images show CubeSats each with a unique configuration of deployed cylindrical antennas and/or booms. Most are linear structures, but the bottom row of images shows that some of the structures have curvature.

4 SIMULATED CUBESAT PHOTOMETRIC SIGNATURES

Our analysis indicates that these unique configurations of wire antennas and/or cylindrical boom structures create variations in the brightness of reflected sunlight that can be used as a means of CubeSat characterization and discrimination. To demonstrate this, we simulate reflected-sunlight signatures of three archetypical CubeSats, one with no antennas at all and two others with the different wire-antenna configurations shown in Figure 2.

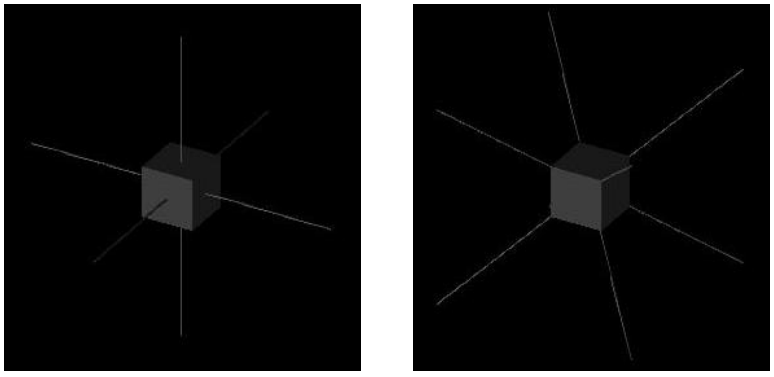

Figure 2. Schematic illustrations of the two CubeSats antenna configurations simulated in this study: six “face-normal” antennas (left panel) and eight “vertex-radial” antennas (right panel). The cubical main bodies are identical in each case.

4.1 Simulation Assumptions and Parameters

These limited simulations aim to qualitatively reproduce CubeSat's as observed by Maui-based Advanced Electro-Optical System (AEOS) 3.6m telescope's Visible Imager (VISIM) instrument using the photometric Bessel I-band filter which spans the 725–925 nm spectral range (see [1] for more details). The simulation software calculates the brightness of reflected sunlight from the CubeSats using a method similar to that in the *Time-Domain Analysis Simulation for Advanced Tracking* (TASAT) software system, and employs bi-directional reflectance distribution function (BRDFs) parameters measured and tabulated by Satellite Assessment Center (see [2, 3, 4] and references therein). However, instead of performing a complete ray-tracing calculation, as in TASAT, these simulations handle the self-shadowing and self-masking of the CubeSats in an approximate manner, in which the effects of the cubical main-body shadowing and obscuring the antennas are accounted for, but not vice versa. This approximation saves significant computation time, and suffices for this study because the surface area of each antenna is much smaller than the surface area of each cube face.

The main bodies of the simulated CubeSats are perfectly cubical with vertex-to-vertex edge lengths of 20cm. Each of the six faces is assumed to have 75% of its area covered by solar array panel (SatAC/TASAT BRDF #0023: "Silicon Sun-side Solar Cell") and 25% by aluminum (SatAC/TASAT BRDF #0046 "Aluminum Alloy 5456-H116 Mill Finish"). The wire antennas are deployed in two basic configurations: "face-normal" antennas that emanate from the center each of the cube's six faces with their long dimension lying perpendicular to the face, and "vertex-radial" antennas emanating from each of the cube's eight vertices with their long dimension lying along the radial direction from the cube's center. Each wire antenna has a length of 25 cm and diameter of 3 mm and assumed to be composed of steel (SatAC/TASAT BRDF #0068 "Steel, HSLA, US Corten A"). Figure 2 illustrates the two CubeSat antenna configurations.

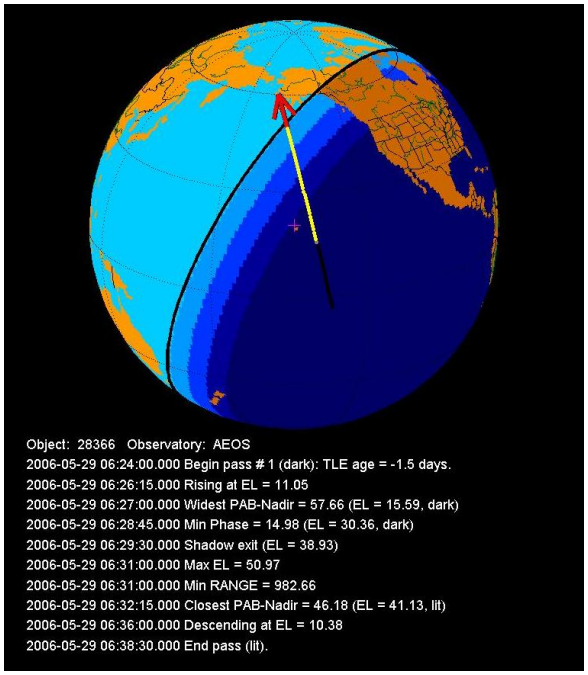

Figure 3. Pass used for the simulated CubeSat photometric observations in this study. The globe shows the solar-illuminated Earth looking straight down on Maui. The over-plotted ground-track shows the path of the satellite as it traverses over the observatory, illustrated in black when the object is in Earth-shadow and yellow when fully sunlit. The red arrow indicates the direction of motion.

The software calculates the brightness as a function of time as the CubeSats pass over the AEOS telescope. As a first step, it propagates orbital trajectories using input two-line element sets to generate the required

pass parameters (such as object position, rise and set times, etc). Figure 3 shows the pass selected for the simulations, corresponding to an actual AEOS observation of the LatinSat-D CubeSat (SCN 28366) on 2006 May 29. Each simulated CubeSat has the same exact orientation during the pass over Maui, spinning at a rate of 0.25 rpm about a randomly-chosen inertial axis selected not to correspond to any axis of body symmetry.

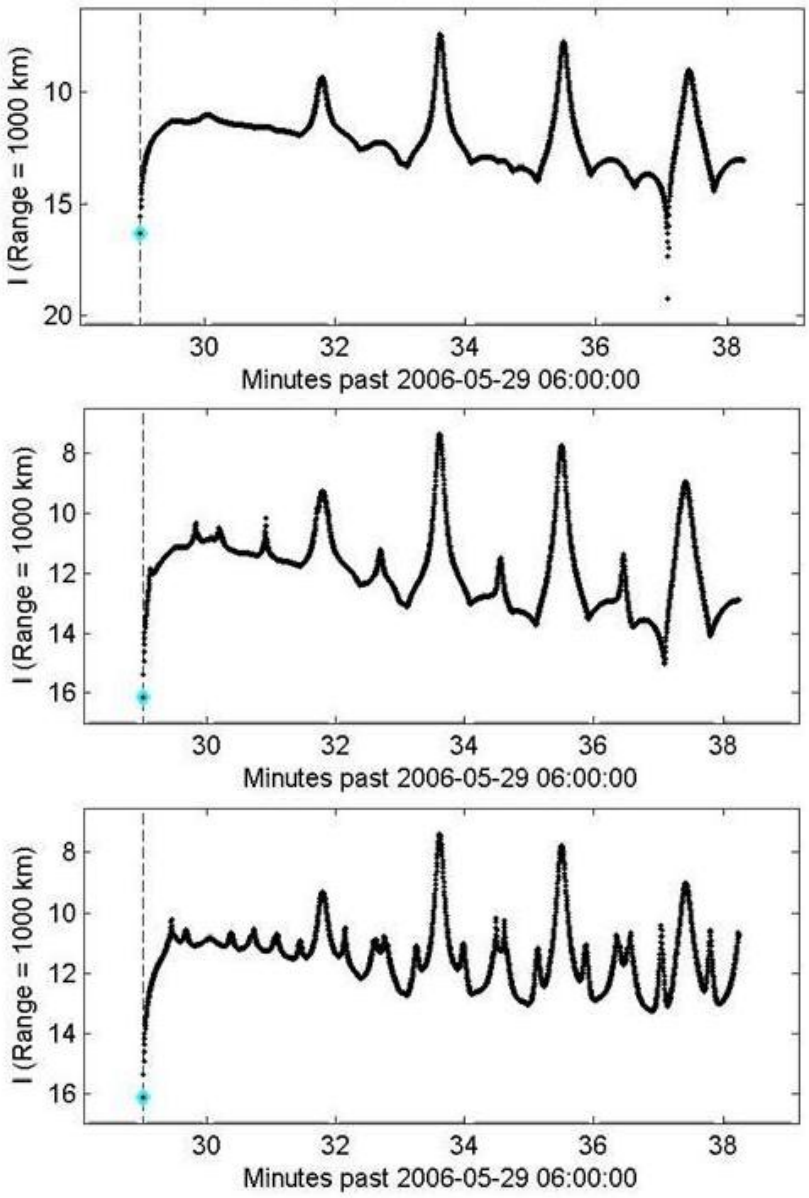

Figure 4. Photometric signatures for the three simulated CubeSats. The horizontal axes show time during the pass illustrated in Figure 3. The vertical axes show the brightness of reflected sunlight measured in I-band stellar magnitudes, with the object-to-observatory range normalized to 1000km. Blue diamonds indicate the first detectable point, which occur just as the satellites exit Earth's shadow. The top panel shows the signature for the simulated CubeSat with no antennas, and indicates that four glints occur from the main-body faces. The middle panel shows the signature for the CubeSat with six face-normal antennas, and shows additional smaller amplitude glints occurring mid-way between the main-face glints, as well as at other times. The bottom panel shows the signature for the CubeSat with eight vertex-radial antennas, showing many additional glints occurring before and after the main-face glints, as well as at other times.

4.2 Simulated CubeSat Photometry

Figure 4 shows the brightness of reflected sunlight as a function of time for the three simulated CubeSats. The top panel shows the signature for a CubeSat with no antennas, and shows evidence of four glints from the main faces of the spinning cube. These glints have amplitudes of 2 to 5 stellar magnitudes. The middle panel shows the signature for a CubeSat with six face-normal antennas (see left panel of Figure 2). It shows glints at these same four times during the pass, as it should because this CubeSat has the same main body and spinning attitude as in the previous simulation, and its faces should glint at exactly the same times. The middle panel also shows additional smaller amplitude glints occurring mid-way between the main-face glints, as well as at other times, in a relatively evenly-spaced sequence along with the main-face glints. These smaller-amplitude glints arise from sunlight reflecting from the face-normal antennas. Furthermore, a careful inspection of the middle panel indicates the four main glints have slightly brighter peak brightness than in the top panel, meaning that face-normal antenna glints must be occurring at the same time as the glints from the main faces themselves. The bottom panel shows the signature for a CubeSat with eight vertex-radial antennas(see right panel of Figure 2). In this case there are many additional glints occurring just before and after the four main-face glints, as well as at other times. A careful inspection of the bottom panel also indicates the four main glints have the same peak brightness amplitude as in the top panel, meaning that vertex-radial antennas glints do not occur at the same time as the glints from the main faces themselves.

Notably, the lower two panels of Figure 4 show that isolated antenna glints have amplitudes of 0.5 to 2 stellar magnitudes and are generally much dimmer than glints from the main faces. Of course, the exact brightness of the antenna glints depends sensitively on the properties of these wire structures. For instance, increasing the diameter of the simulated antennas from 3 mm to 5 mm increases their reflective areas by a factor of $\approx$2.8, and brightens the glints by roughly 1 magnitude.

4.3 Cube Face and Wire Antenna Glint Conditions

The simulated signatures illustrate that glints of sunlight from antennas do indeed create tell-tale patterns that potentially provide a means of using temporal reflected-sunlight photometry as a means of CubeSat characterization and discrimination. A better understanding of these patterns can be gained by examining the geometric conditions under which mirror-like reflections occur from both the main-body faces and the wire antennas of the CubeSats. The mathematical details of these glint conditions are discussed in [5] and briefly described here. Flat surfaces, such as the six main-body faces of a CubeSat, glint when the angle of incoming sunlight equals (or nearly equals) the outgoing angle towards an observer, i.e., when the "specular condition" for the surface is satisfied. Another way to express this specular condition is that the normal vector to the face coincides with the "phase angle bisector" (PAB), which is defined as the unit direction vector midway between the satellite-to-Sun and satellite-to-observer vectors. On the other hand, a cylindrical wire antenna glints when its long axis lies perpendicular to the PAB. These two geometrical effects lead the distinct patterns of glints apparent in Figure 4.

Figure 5 illustrates simulated Cubesats at times of glint events. For illustrative purposes, the wire antenna diameters have been enlarged by a factor of ten to better enable the visualization of when and where the glints occur. The top panels show the configuration with six face-normal antennas, indicating that a main-face glint always coincides with face-normal antenna glints (top left) but that face-normal antenna glints do not necessarily coincide with main-face glints (top right). This leads the effects apparent in the middle panel of Figure 4, where all of the main-face glints were slightly enhanced in amplitude by simultaneous antenna glints, but isolated antenna glints occur roughly mid-way between the main-face glints. The bottom panels of Figure 5 show the configuration with eight vertex-radial antennas, indicating that main-face glints never coincide with the antenna glints. This mutually exclusive glint behavior leads to the general pattern of glints apparent in the bottom panel of Figure 4, where the antenna glints occur before and after the four main-face glints. Other simulations indicate that this pattern of antenna glints "bracketing" main face glints is actually related to the fact that the antennas lie along directions that are not normal to any of the faces. In this regard, similar signatures with such bracketing glint patterns would be also expected from CubeSats with "edge-radial" antennas, for instance, which emanate radially outward from the cube edges.

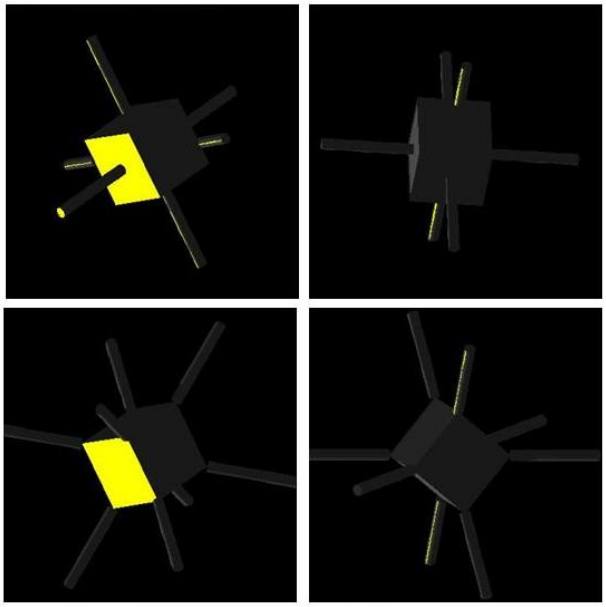

Figure 5. Schematic illustrations of CubeSats at times of glint events, shown with the wire antenna diameters enlarged by a factor of ten for visual clarity. Yellow shading indicates regions where the specular condition is approximately satisfied and the glints originate. The top panels show a CubeSat with six face-normal antennas, indicating that a main-face glint always coincides with antenna glints (top left) but that face-normal antenna glints do not always coincide with main-face glints. The bottom panels show the configuration of eight vertex-radial antennas, indicating that main-face glints never coincide with the antenna glints.

5 SELECTED AEOS VISIM OBSERVATIONS

The simulations described above do not represent accurate or best-fit models of actual observations of any specific CubeSats. That kind of detailed model analysis surpasses the scope of this investigation. However, some observed photometric brightness vs. time signatures do indeed show similar morphology to even the limited simulations performed in this analysis, suggesting that using patterns of glints as a method of CubeSat discrimination is worthy of additional study.

Figure 6 shows an artists illustration of the LatinSat-B cubical satellite (SCN 27607) taken from the web, and the I-band signature observed by the AEOS VISIM instrument on 2003 Sep 20. The signature shows large amplitude glints ($\geq$ 2 magnitudes), likely from the main body faces, as well as smaller amplitude glints ($\approx$0.5 magnitude) that tend to bracket the main face glints. Suggestively, four of the antenna-like structures on the artist's depiction of this satellite have an "edge-radial" configuration which the simulations indicate can produce this bracketed glint signature, as discussed in the previous section.

Figure 7 shows a pre-launch photograph of the LatinSat-D satellite (SCN 28366) along with three AEOS VISIM I-band signatures. All three signatures show large amplitude glints ($\geq$ 2 magnitudes), likely from the main body faces. However, these signatures only show intermittent small-amplitude glints. This may be caused by the facts that the antennas on this CubeSat are directing inward from the cube vertices (rather than radially outward in the simulation) and/or that the antennas are much smaller relative to the main faces compared to the simulations. Notably for this CubeSat, the peak-to-peak time interval for the large amplitude glints grows from $\approx$70 seconds up to $\approx$100 seconds during the 10 month period spanned by these observations, possibly indicating a deceleration of rotational motion.

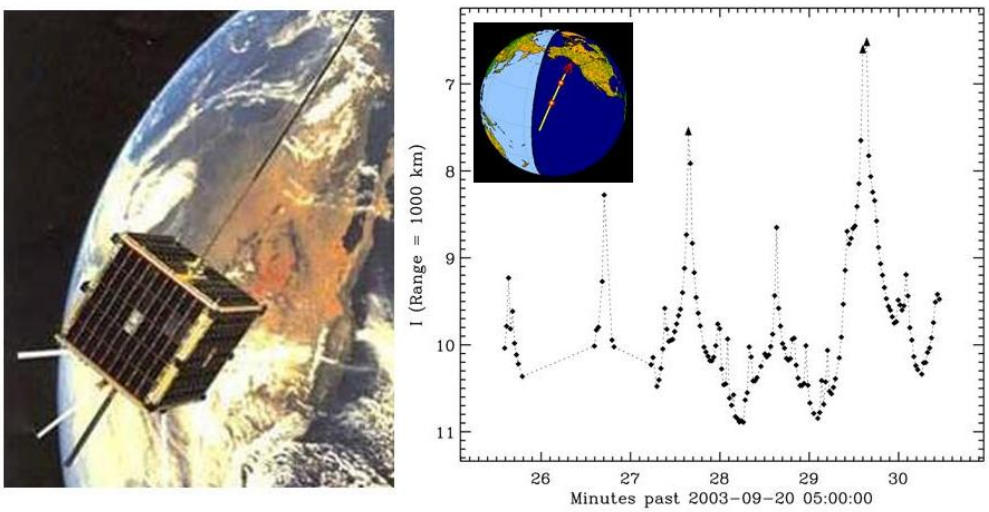

Figure 6. An artists illustration of the LatinSat-B satellite (left panel) and the I-band photometric signature observed by the AEOS VISIM instrument on 2003 Sep 20 with an inset illustration of the pass ground-track (right panel).

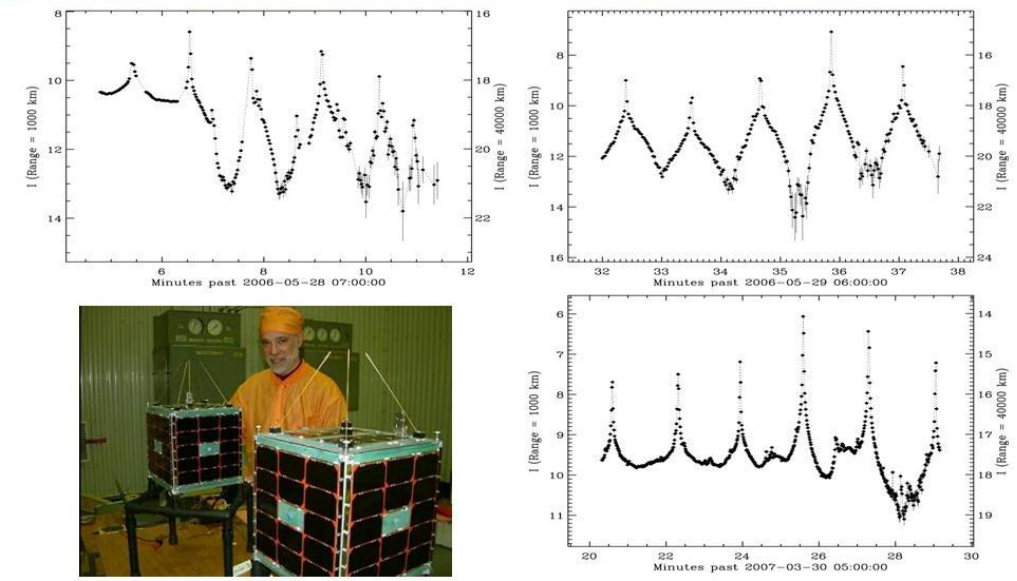

Figure 7. A pre-launch photograph of the LatinSat-D satellite (lower left) and three I-band photometric signatures observed by the AEOS VISIM instrument on 2006 May 28 (upper left), 2006 May 29 (upper right) and 2007 Mar 30 (lower right).

6 CONCLUSIONS

Different CubeSats launched within a group often have many similarities in structure, but most are distinguished by a unique configuration of wire antennas and booms. Our limited simulations indicate that these shiny wire structures can serve as discriminating identifiers for these non-resolvable objects, because they create tell-tale photometric patterns of glints in reflected sunlight. More research promises to provide a means of remotely diagnosing the size and curvature of these antenna and boom structures as well as their orientation relative to the main cubical satellite body.

7 REFERENCES

1. Hall, D.T., Africano, J.L, Lambert, J.V., and Kervin, P.W., "Time-Resolved I-band Photometry of Calibration Spheres and NaK Droplets", *J. Spacecraft and Rockets*, Vol. 44, No. 4, pp. 910–919, 2007.
2. Maxwell, J.R., Beard, J., et.al., "Bi-directional Reflectance Model Validation and Utilization", *Air Force Avionics Laboratory Technical Report*, AFAL-TR-73-303, October 1973.
3. Rigby, F., Doerr, S., and Hulce, D., "Maxwell-Beard Model Improvement", *SAIC Report*, prepared under AF Contract F29601-00-0011 Task Order 10, Nov. 2001.
4. Riker, J., and Butts, R., "The Time-Domain Analysis Simulation for Advanced Tracking (TASAT) Approaches to Compensated Imaging", *SPIE* Vol.1688, Atmospheric Propagation and Remote Sensing, 1992.
5. Hall, D., Calef, B., Knox, K., Bolden M., and Kervin, P., "Separating Attitude and Shape Effects for Non-resolved Objects" *The 2007 AMOS Technical Conference Proceedings*, Kihei, HI, 2007.